PHOTONICS Research

Topological photonic crystal of large valley Chern numbers

Xiang Xi, Kang-Ping Ye, and Rui-Xin Wu*

School of Electronic Science and Engineering, Nanjing University, Nanjing 200023, China
Corresponding author: rxwu@nju.edu.cn

The recent realizations of a topological valley phase in a photonic crystal, an analog of gapped valleytronic materials in an electronic system, are limited to the valley Chern number of one. In this paper, we present a type of valley phase that can have a large valley Chern number of two or three. The valley phase transitions between the different valley Chern numbers (from one to three) are realized by changing the configuration of the unit cell. We demonstrate that these topological phases can guide the wave propagation robustly along a sharply bent domain wall. We believe our results are promising for the exploration of new topological phenomena in photonic systems.   © 2020 Chinese Laser Press

https://doi.org/10.1364/PRJ.396872

1. INTRODUCTION

Photonic topological states, rooted in the studies of topological insulators in electronic systems, have opened up an intriguing way to control the motion of electromagnetic (EM) waves. There has been a lot of interest in the topological edge states resulting from the topological phases that can route the wave propagation, overcoming the backscattering and remaining robust against defects [1–5]. Many photonic topological phases have already been proposed, such as the quantum Hall (QH) phase [2–11], the quantum spin Hall (QSH) phase [12–18], and the quantum valley Hall (QVH) phase [19–33].

Symmetry plays a key role in the design of the topological phases of photonic crystals (PCs). In the honeycomb structured magnetic PCs, for example, breaking the time-reversal (TR) symmetry will gap a pair of Dirac cones at high symmetry K and K' points, so that the Berry curvature has the same sign at these points and yields a nonzero topological invariant number, the Chern number, $|C| = 1$. If the Dirac points are away from the high symmetry points, the Berry curvature will have more extremes around the K and K' points, and the Chern number will be greater than one [6,7]. Similarly, the QVH phase is related to the breaking of inversion symmetry, which introduces a binary degree of freedom (DOF) in the PCs, an analog of the valley DOF spintronics in the electronic system. Valley labels the energetically degenerate yet inequivalent points in momentum space [20]. This new DOF also opens the Dirac cones at high symmetry K and K' points, but the Berry curvature at these two points has an opposite sign; therefore, the Chern number of the bandgap will be zero. However, the valley Chern number C_v, defined at the valley points, is nonzero [22,24]. The topological valley phase gets rid of the

limitation of a bias magnetic field, opening a path toward the topological phase in all-dielectric PC [19–33]. To date, the QVH phase in PCs is limited to $|C_v| = 1$. A natural question is whether or not the QVH phase can have a large valley Chern number.

In this work, we report what we believe, to the best of our knowledge, is a new type of valley phase where the valley Chern number can be $|C_v| = 1$, 2, or 3, depending on the configuration of the unit cell. The variations of the valley Chern number are achieved by expanding or shrinking one set of rods of the hexamer. These new QVH phases are characterized by the Berry curvature in the first Brillouin zone, and further proven by the edge states at the domain wall according to the bulk-edge correspondence [34,35]. Note that the number of edge states is the same as the difference in the valley Chern numbers across the domain wall. The robust wave transmissions of these QVH phases are demonstrated by the Z-shaped domain wall. Having band gaps with larger valley Chern numbers greatly expands the phases available for topological photonics.

2. TOPOLOGICAL VALLEY STATES WITH LARGE VALLEY CHERN NUMBERS

A. Dirac Points Away from the High Symmetry Point

Consider that the PC structure is fabricated by the artificial molecules, as shown in Fig. 1(a). Each molecule, composed of six neighboring rods, is a hexamer in the background air. Suppose the rods are made of yttrium iron garnet (YIG), whose relative permittivity and permeability are $\varepsilon_r = 15.26$ and $\mu_r = 1$, respectively, at microwave frequencies. The molecules are arranged in the hexagonal lattice, and the lattice constant is $a = 10\sqrt{3}$ mm. The radius of the rods is $r = 0.2a$.
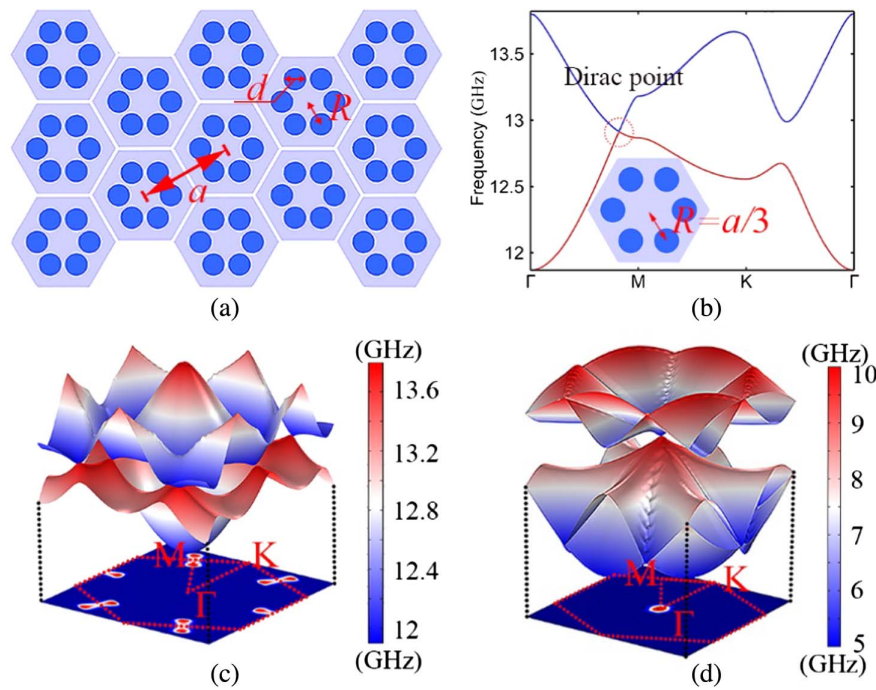
Fig. 1. (a) Schematic of 2D PC structure, composed of hexamers of six ferrite rods and embedded in the air background. The white lines denote the edge of a unit cell. (b) Band structure of the PC at $R = a/3$. A Dirac point is away from the high symmetry points in the first Brillouin zone. (c) 3D band structure of the PC. Three pairs of Dirac points are between the two bands in the Brillouin zone. (d) 3D band structure of Ref. [13]. One pair of Dirac points presents at the Γ point.

The dimension of the molecule is measured by the distance between the rods' center and the center of the unit cell, denoted by R in the figure.

Figure 1(b) plots the band structure at $R = a/3$. The calculations were performed by commercial finite element method solver COMSOL Multiphysics and its Wave Optics Module. In the calculation, the unit cell was used and the Floquet periodic boundary condition was applied to it. A Dirac point presents at the frequency of 12.9 GHz in the band structure. This point is a general point in k-space, not at a high symmetry point, as other works have reported [19–33]. We note the arrangement of the hexamer in the unit cell is different from that in Ref. [13], where the hexamer has an additional rotation of $\pi/6$. This configuration keeps the hexagonal structure even when the rods expand or shrink, unlike in Ref. [13] where the structure changes from hexagonal to honeycomb at $R = a/3$ where the Dirac point is present. Due to the symmetry of the system, three pairs of Dirac points emerge in the first Brillouin zone, as displayed in Fig. 1(c). In contrast, only one pair of Dirac points is in the configuration of Ref. [13] at the Γ point, as displayed in Fig. 1(d). The increment of the fold of degeneracy results in a large Chern number of the bands when they are gapped [6,7].

B. Valley Phase of Large Valley Chern Number
To gap the Dirac points, one can break the time-reversal symmetry or the space-inversion symmetry. After the symmetry-breaking operation, the Dirac points are opened, and each degeneracy lifting contributes a Berry flux of magnitude π in each band [2–5], leading to a peak in the Berry curvature.

Each peak contributes a Chern number $|C| = 1/2$. When the total Berry flux adds up to 2π, the Chern number will be $|C| = 1$ [8].

Here, we gap the Dirac points by breaking the inversion symmetry of the system. Shrinking or expanding the distance R of the set of rods (marked in red) and keeping the other set (marked in blue) unchanged, the rotation symmetry of the system changes from original C_6 to C_3. Meanwhile, the inversion symmetry of the system is broken; that is, the unit cell does not keep its original form under the transform of (x, y) to $(-x, -y)$ for two-dimensional (2D) systems. This operation opens a full bandgap at the Dirac point, and the valleys appear at the $K(K')$ point. As displayed in Fig. 2(a), the extreme value presents in the band above the gap (upper band) and below the gap (lower band). However, the valleys are different from those previously reported [19–33].

To show the difference, the Berry curvature and the valley Chern number were numerically calculated. The Berry curvature of the nth band is defined as $\Omega_n(\mathbf{k}) = \nabla_\mathbf{k} \times A_n(\mathbf{k})$ [4,36], where $A_n(\mathbf{k}) = i\langle \mu_{n,\mathbf{k}} | \nabla_\mathbf{k} | \mu_{n,\mathbf{k}} \rangle$ is the Berry connection and $\mu_{n,\mathbf{k}}$ is the Bloch state. The efficient algorithm [37] was used in the calculation of the Berry curvature over the Brillouin zone. In the zone, each peak of the curvature contributes to the Chern number $|C| = 1/2$ [8], and the valley Chern number is obtained by counting the number of peaks. As an illustration, Fig. 2(b) plots the Berry curvature of the lower band in the first Brillouin zone. We see one peak presents at the valley and the other three peaks around it. Because the system preserves time-reversal symmetry, the peaks up and down are in the same numbers, and thus the Chern number of the band
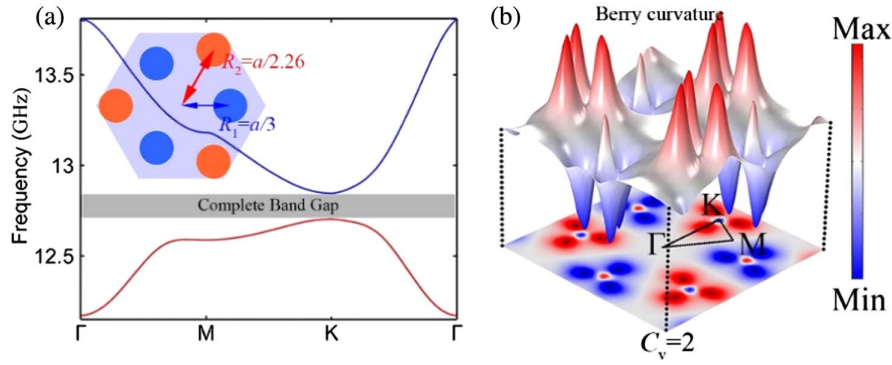
Fig. 2. (a) Band structures of the PC at $R_1 = a/3$ and $R_2 = a/2.26$. (b) Berry curvature in the first Brillouin zone. Curvature is opposite around the K and K' points, and the valley Chern number $C_v = C_k - C_{k'} = 1 - (-1) = 2$.

is zero. However, the band can be characterized by a valley Chern number because the Berry curvature is distinguished at K and K' valleys. Figure 2(b) shows three peaks up and one peak down near the K valley, but near the K' valley shows one peak up and three peaks down. Therefore, the valley Chern number of the band is $C_v = C_k - C_{k'} = 1 - (-1) = 2$. Simply rotating the original unit cell by 60° will reverse the valley Chern number from $C_v = 2$ to $C_v = -2$ [38].

A further demonstration of the system having a larger valley Chern number is to check the number of topological edge states at the boundary. According to the bulk-edge correspondence [34,35], the number of edge states between two topologically distinct domains should be the difference of the valley Chern number across the boundary. We construct a domain wall where two domains have opposite valley Chern numbers: $C_v = 2$ ($C_k = 1$ and $C_{k'} = -1$) and $C_v = -2$ ($C_k = -1$ and $C_{k'} = +1$). The two domains have identical parameters, as in Fig. 2(a), but one domain takes a rotation of 60° for its unit cells. Across the domain wall, the differences in the valley Chern number should be $|\Delta C_v| = 2$ at $K(K')$ point. Indeed, two edge states emerge inside the bandgap, as shown in Fig. 3(a). The insets display the edge modes at the dots of the edge dispersion curves. The electric field is localized near the domain wall and decays rapidly away from the wall. As a representative example, Fig. 3(b) displays the transmission spectra of the Z-shape bend. The waves along the domain wall are against the disorders, as shown in the insets of Fig. 3(b).

The figure shows that the valley edge states can guide the waves around a sharp bend smoothly without reflection in the single-mode region; however, some reflection occurs in the multi-mode region because the intervalley scattering is increased.

3. VALLEY PHASES OF DIFFERENT VALLEY CHERN NUMBERS

The valley phases of the PC depend on the expansion or shrinking of one set of rods. One can identify the different phases by their eigenstates or their valley Chern numbers. As an example, we keep the blue set of rods at $R_1 = a/3$, while expanding the red set of rods to $R_2 = a/2.36$, as shown in the inset of Fig. 4(a). In this situation, the bandgap and energy valley appear in the band structure, as shown in Fig. 4(a). At the valley, the phase of the electric field E_z and the power flow are illustrated in Fig. 4(b). Similar to the reported valley states, we see the pseudospin of a large valley Chern number in the figure; the power flows are circulating counterclockwise outside one set of rods, but are inside the other set of rods. Generally, the valley pseudospin around the K' point can be distinguished well from the K point since the vortex chirality is reversed [30]. If the source that matches the vortex chirality of a specific valley, it will excite the corresponding valley states and the other valley state will be suppressed [32]. It provides an intuitive, easy way to confirm the existence of the pseudospin in our system. We first performed full-wave simulations to get the field
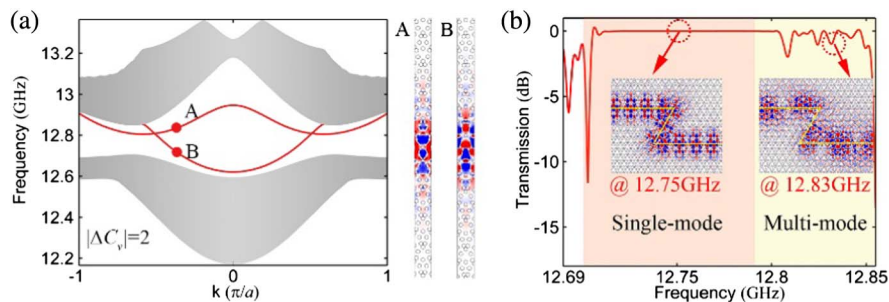
Fig. 3. Topological edge state of valley Chern number $C_v = 2$. (a) Projected band structures for the valley Chern difference $|\Delta C_v| = 2$ at $K(K')$ point across the domain wall. Insets are the distributions of E_z at the given points A and B in the band structure. (b) Transmission spectra of Z-shape corners in the frequency range of 12.69–12.85 GHz. The red and yellow regions correspond to the single-mode and multimode regions, respectively. The insets are the E_z field distributions at the frequencies in the single-mode and multimode regions.
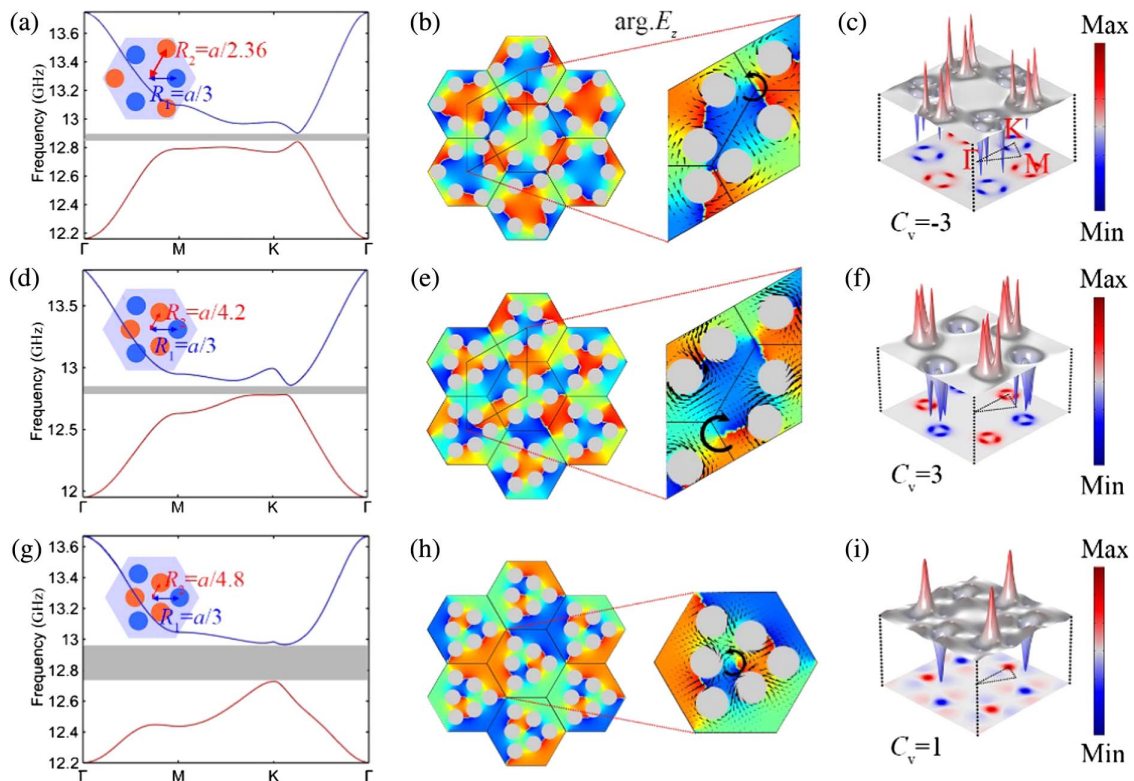
Fig. 4. Band structures, phase and power flow distribution, and corresponding Berry curvature of the PC, where R_1 is fixed at $a/3$, (a) $R_2 = a/2.36$ and valley Chern number $C_v = -3$, (b) $R_2 = a/4.2$ and $C_v = 3$, and (c) $R_2 = a/4.8$ and $C_v = 1$. Arrow inserted in the phase distribution indicates the Poynting vector.

distribution in the PC by the chiral source composed of four antennas [14]. The source can provide the positive or the negative orbital angular momentum (OAM), as shown in Fig. 5(a). Then, we did a 2D spatial Fourier transformation to get the field spectrum in the momentum space. The results are displayed in Figs. 5(b) and 5(c). We observe that the chiral source with positive OAM excites the field located near K points in momentum space, but the source with negative OAM excites the field near the K' points. The field center is slightly off the K and K' points, as shown in the inset of Figs. 5(b) and 5(c), because the valley points of the large valley Chern number shift

from the high symmetry points. The results confirm that the valleys have pseudospins, and the pseudospin near the valleys K and K' has a different orientation.

A direct reflection of the valley phase is the Berry curvature, as shown in Fig. 4(c). We see three peaks are down near the K point, while three peaks are up near the K' point. Thus, the valley Chern number is $C_v = C_k - C_{k'} = -3/2 - (3/2) = -3$, a negative number. The number of peaks near the valleys is different from the conventional valley states. The reason is associated with the configuration in the unit cell. The phase of E_z and power flow circulating indicate the red and blue rods can be
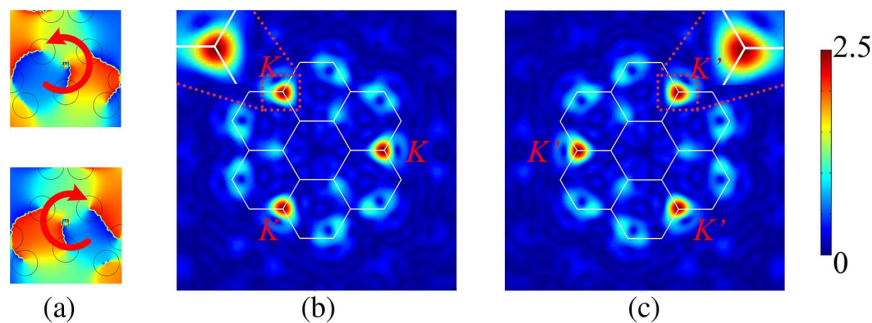
Fig. 5. Electric field distribution in momentum space. (a) Chiral sources carry positive and negative OAM. Colors are the phase of electric field excited by the source in the center. Arrows show the direction of OAM: the counterclockwise arrow represents the positive OAM and the clockwise arrow represents the negative one. (b) Field excited by the chiral source with positive OAM, where the field is strongly localized at point K. (c) Field excited by the source with negative OAM, where the field is strongly localized at point K'. Panel insets are the close look near the point K or K'.

considered as two different trimers, the small trimer and the big trimer. The trimers are in inequivalent positions of the unit cells, forming A and B sublattices. The difference between R_1 and R_2 plays a role in the staggered potential between two sublattice Δ, which is similar to applying the rods with a different diameter in the unit cell in Ref. [24] or the rods of different height in Ref. [21]. The values of R_1 and R_2 determine the staggered potential Δ. For example, the staggered potential is zero at $R_1 = R_2$, but it is nonzero at $R_1 \neq R_2$. The staggered potential Δ between the sublattices opens a gap at the Dirac points, which affects the valley Chern number.

Changing the R value of one subset may transform the valley state to other phase. Supposing we reduce the dimension of the red subset to $R_2 = a/4.2$. Once again, the full bandgap and valleys present in the band structure [Fig. 4(d)]. The phase distribution and power flows [Fig. 4(e)] show the red and the blue trimers can be recognized as two sublattices. However, the big and small trimers exchange their position in the unit cell, which results in an opposite staggered potential Δ compared to the one in Fig. 4(b). It also can be observed in the Berry curvature [Fig. 4(f)], where the peaks upward and downward are exchanged between K and K' points in Fig. 4(c). Thus, the valley Chern number at $R_2 = a/4.2$ is $C_v = C_k - C_{k'} = 3/2 - (-3/2) = +3$, a positive number.

Further shrinking the dimension of the red set will strengthen the coupling between the six rods, and all the rods in the unit cell function as a whole, the hexamer. As displayed in Fig. 4(h), when R_2 takes $a/4.8$, the phase distribution of the electric E_z concentrates at the hexamer and the power flow is counterclockwise around the central point of the unit cell, which is similar to the valley phase in Ref. [27]. The Berry curvature of the band below the bandgap shows only one peak at the $K(K')$ points, and the valley Chern number is $C_v = 1$.

The different phases of the large valley Chern number are related to the band inversion happening in the band structure, which can be identified by the opening–closing–reopening of the full bandgap. Figure 6 gives the variation in eigenfrequencies of the valleys when we continuously vary R_2 while fixing

$R_1 = a/3$. With the variation of R_2, the valleys experience several instances of opening and closing, indicating the full bandgap creating and disappearing. By gradually increasing R_2 to $a/2.36$ from $a/3$, where there is a Dirac point, a full bandgap opens at about $a/2.54$. The valleys present away from the high symmetry point in the momentum space and the valley Chern number is -3 [Fig. 4(c)]. Further increasing the R_2, the bandgap closes at about $a/2.32$ and then reopens once again. The process reverses the peaks of Berry curvature, which happens at a general point in the momentum space. Thus, the valley Chern number takes the opposite sign $+3$. After one more increase of R_2, at about $a/2.3$, the bandgap closes and then opens again at $K(K')$ points, which leads to a new peak at $K(K')$ point. The new peak is in the opposite direction of the neighboring three peaks [Fig. 2(b)], resulting in a valley phase transition from $C_v = 3$ to $C_v = 2$. Similarly, when R_2 decreases from $a/3$, the full bandgap opens at about $R_2 = a/3.66$. Further decreasing R_2 to $a/4.8$, the peaks of the Berry curvature near the $K(K')$ points [Fig. 4(f)] shrink to the $K(K')$ points; therefore, the valley Chern number is one when R_2 is over $a/4.8$.

The valley Chern numbers can further be proven by the number of the topological edge states at the domain wall. Again, we make the domain wall between the two PCs with opposite valley Chern numbers. Figure 7(a) shows the band structure of the two domains with a valley Chern number of $C_v = 1$ ($C_k = 1/2$ and $C_{k'} = -1/2$) and $C_v = -1$ ($C_k = -1/2$ and $C_{k'} = +1/2$). The two domains have identical geometrical parameters, as in Fig. 4(g), but one domain shrinks the red set while the other shrinks the blue set. We observe one edge state appearing in the bandgap, because the difference in the valley Chern number $|\Delta C_v|$ across the domain wall is one at $K(K')$ point. Figure 7(c) shows that the wave propagates along a Z-shaped domain wall in the frequency range of 12.7–12.95 GHz. At the edge modes, the wave is localized at the domain wall and robust against the sharp corners of the domain wall. Similarly, for the domain wall created by the PCs of valley Chern number $C_v = -3$ and $+3$, where structure parameters are $R_1 = a/3$ and $R_2 = a/4.2$ for one domain, and $R_1 = a/4.2$ and $R_2 = a/3$ for the other domain, three edge states present in the projected band structure, as shown in Fig. 7(b). The number of edge states is consistent with the differences of the valley Chern number across the domain wall; $|\Delta C_v| = 3$ at $K(K')$ point. For these edge states, Fig. 7(b) plots the field profile of the modes, and the field always concentrates on the domain wall, which functions as a waveguide. The robustness of the wave propagation along the domain wall in the frequency range of 12.78–12.87 GHz is shown in Fig. 7(d). We see the wave is efficient going across the sharp corners of the Z-shaped domain wall. We should note that because of the multiple edge modes at a given frequency, the robustness of the wave propagation may be weaker in some cases of disorders. Even so, the multiple edge modes of the waveguide may be applied to increase the coupling efficiency of photonic devices [39], such as demultiplexers [40] and 3 dB power splitters [41]. The reconfiguration of edge modes number provides an easy way to realize tunable devices, such as a dispersion tuning waveguide, where single or multiple modes
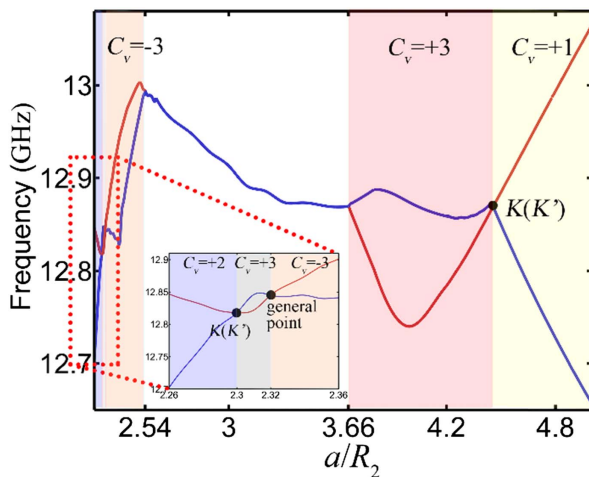
Fig. 6. Variation of the valley frequency with varying R_2 when R_1 is fixed. The valley Chern number C_v remains unchanged in the region of the same color.
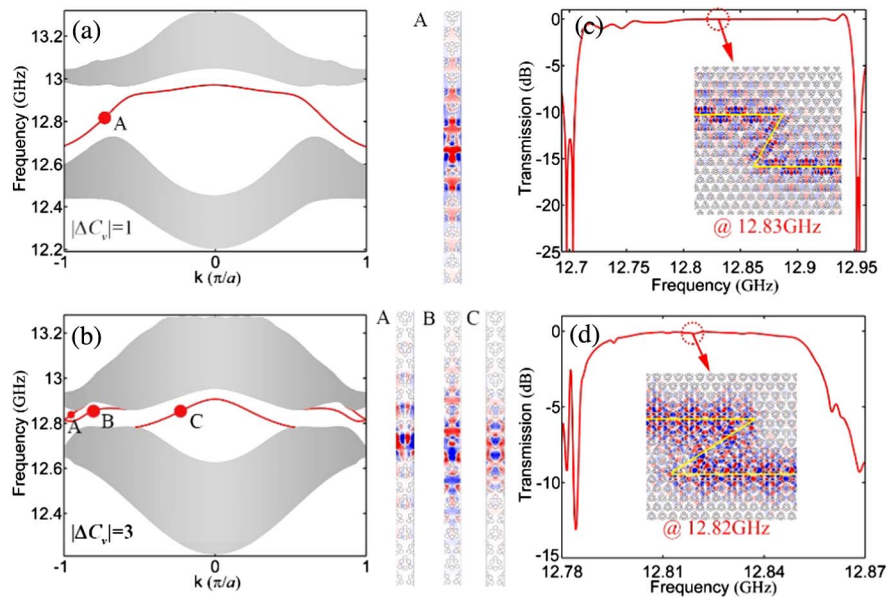
Fig. 7. Topological edge state of valley Chern number of $C_v = 1$ and 3. Panels (a) and (b) are the projected band structures for the valley Chern number difference across the domain wall, respectively, $|\Delta C_v| = 1$ and 3 at $K(K')$ point. The number of edge states present in the bandgap is the same as the valley Chern number difference. The panel insets are the distributions of E_z at the given points in the band structure. The fields are all localized at the domain wall. (c) and (d) Transmission spectra of Z-shaped topological domain wall for valley Chern number difference $|\Delta C_v| = 1$ and 3 at $K(K')$ point, respectively. Simulated E_z field distributions are inserted. The yellow curves represent the energy flows.

can be switched by simply rotating the original unit cell by 60°. The topological valley phases get rid of the magneto–optical effects, which are typically weak at optical frequencies, and then they can be extended to even higher frequencies. Therefore, the topological phases of a large valley Chern number may have potential applications in topological photonic integrated circuits and devices [29,33] because of their ease of implementation.

4. CONCLUSION

In conclusion, we have proposed and theoretically demonstrated what we believe, to the best of our knowledge, is a new type of valley Hall phase in 2D photonic crystal, which is made of the hexamers of dielectric rods and has a large valley Chern number. By simply shrinking or expanding one set of rods in the hexamer, we realize a valley phase transition from the valley Chern number of one to three. The multiple edge states further demonstrate our valley phases with large valley Chern numbers, which are perfectly compatible with the bulk-edge correspondence. Robustness of the edge modes is demonstrated by the wave transmission along the domain wall of the Z-shaped form. We believe our study provides new opportunities in topological photonics, according to practical requirements.

Disclosures. The authors declare no conflicts of interest.

REFERENCES

1. T. Ozawa, H. M. Price, A. Amo, N. Goldman, M. Hafezi, L. Lu, M. Rechtsman, D. Schuster, J. Simon, and O. Zilberberg, "Topological photonics," Rev. Mod. Phys. **91**, 015006 (2019).
2. S. Raghu and F. D. M. Haldane, "Possible realization of directional optical waveguides in photonic crystals with broken time-reversal symmetry," Phys. Rev. Lett. **100**, 013904 (2008).
3. F. D. M. Haldane and S. Raghu, "Analogs of quantum-Hall-effect edge states in photonic crystals," Phys. Rev. A **78**, 033834 (2008).
4. Z. Wang, Y. D. Chong, J. D. Joannopoulos, and M. Soljačić, "Reflection-free one-way edge modes in a gyromagnetic photonic crystal," Phys. Rev. Lett. **100**, 013905 (2008).
5. Z. Wang, Y. D. Chong, J. D. Joannopoulos, and M. Soljačić, "Observation of unidirectional backscattering-immune topological electromagnetic states," Nature **461**, 772–775 (2009).
6. S. A. Skirlo, L. Lu, and M. Soljačić, "Multimode one-way waveguides of large Chern numbers," Phys. Rev. Lett. **113**, 113904 (2014).
7. S. A. Skirlo, L. Lu, Y. C. Igarashi, Q. H. Yan, J. Joannopoulos, and M. Soljačić, "Experimental observation of large Chern numbers in photonic crystals," Phys. Rev. Lett. **115**, 253901 (2015).
8. L. Lu, J. D. Joannopoulos, and M. Soljačić, "Topological photonics," Nat. Photonics **8**, 821–829 (2014).
9. A. B. Khanikaev and G. Shvets, "Two-dimensional topological photonics," Nat. Photonics **11**, 763–773 (2017).
10. C. He, X. C. Sun, X. P. Liu, M. H. Lu, Y. L. Chen, L. Feng, and Y. F. Chen, "Photonic topological insulator with broken time-reversal symmetry," Proc. Natl. Acad. Sci. USA **113**, 4924–4928 (2016).
11. Y. Poo, R. X. Wu, Z. F. Lin, Y. Yang, and C. T. Chan, "Experimental realization of self-guiding unidirectional electromagnetic edge states," Phys. Rev. Lett. **106**, 093903 (2011).

12. Z. G. Chen, J. Mei, X. C. Sun, X. Zhang, J. Zhao, and Y. Wu, "Multiple topological phase transitions in a gyromagnetic photonic crystal," Phys. Rev. A **95**, 043827 (2017).

13. L. H. Wu and X. Hu, "Scheme for achieving a topological photonic crystal by using dielectric material," Phys. Rev. Lett. **114**, 223901 (2015).

14. Y. Yang, Y. F. Xu, T. Xu, H. X. Wang, J. H. Jiang, X. Hu, and Z. H. Hang, "Visualization of a unidirectional electromagnetic waveguide using topological photonic," Phys. Rev. Lett. **120**, 217401 (2018).

15. L. Xu, H. X. Wang, Y. D. Xu, H. Y. Chen, and J. H. Jiang, "Accidental degeneracy in photonic bands and topological phase transitions in two-dimensional core-shell dielectric photonic crystals," Opt. Express **24**, 18059–18071 (2016).

16. X. Zhu, H. X. Wang, C. Xu, Y. Lai, J.-H. Jiang, and S. John, "Topological transitions in continuously deformed photonic crystals," Phys. Rev. B **97**, 085148 (2018).

17. R. E. Christiansen, F. W. Wang, and O. Sigmund, "Topological insulators by topology optimization," Phys. Rev. Lett. **122**, 234502 (2019).

18. S. Barik, H. Miyake, W. DeGottardi, E. Waks, and M. Hafezi, "Two-dimensionally confined topological edge states in photonic crystals," New J. Phys. **18**, 113013 (2016).

19. X. D. Xu, W. Yao, D. Xiao, and T. F. Heinz, "Spin and pseudospins in layered transition metal dichalcogenides," Nat. Phys. **10**, 343–350 (2014).

20. J. W. Dong, X. D. Chen, H. Y. Zhu, Y. Wang, and X. Zhang, "Valley photonic crystals for control of spin and topology," Nat. Mater. **16**, 298–302 (2017).

21. Z. Gao, Z. Yang, F. Gao, H. Xue, Y. Yang, J. Dong, and B. Zhang, "Valley surface-wave photonic crystal and its bulk/edge transport," Phys. Rev. B **96**, 201402 (2017).

22. T. Ma and G. Shvets, "All-Si valley-Hall photonic topological insulator," New J. Phys. **18**, 025012 (2016).

23. F. Gao, H. Xue, Z. Yang, K. Lai, Y. Yu, X. Lin, Y. Chong, G. Shvets, and B. Zhang, "Topologically protected refraction of robust kink states in valley photonic crystals," Nat. Phys. **14**, 140–144 (2018).

24. X. D. Chen, F. L. Zhao, M. Chen, and J. W. Dong, "Valley-contrasting physics in all-dielectric photonic crystals: orbital angular momentum and topological propagation," Phys. Rev. B **96**, 020202 (2017).

25. X. D. Chen, F. L. Shi, H. Liu, J. C. Lu, W. M. Deng, J. Y. Dai, Q. Cheng, and J. W. Dong, "Tunable electromagnetic flow control in valley photonic crystal waveguides," Phys. Rev. Appl. **10**, 044002 (2018).

26. X. T. He, E. T. Liang, J. J. Yuan, H. Y. Qiu, X. D. Chen, F. L. Zhao, and J. W. Dong, "A silicon-on-insulator slab for topological valley transport," Nat. Commun. **10**, 872 (2019).

27. L. Zhang, Y. H. Yang, M. J. He, H. X. Wang, Z. J. Yang, E. P. Li, F. Gao, B. L. Zhang, R. J. Singh, J. H. Jiang, and H. S. Chen, "Valley kink states and topological channel intersections in substrate-integrated photonic circuitry," Laser Photon. Rev. **13**, 1900159 (2019).

28. Q. Chen, L. Zhang, M. He, Z. Wang, X. Lin, F. Gao, Y. Yang, B. Zhang, and H. Chen, "Valley-Hall photonic topological insulators with dual-band kink states," Adv. Opt. Mater. **7**, 190036 (2019).

29. Y. Zeng, U. Chattopadhyay, B. Zhu, B. Qiang, J. Li, Y. Jin, L. E. Li, A. G. Davies, E. H. Linfield, B. Zhang, Y. Chong, and Q. J. Wang, "Electrically pumped topological laser with valley edge modes," Nature **578**, 246–250 (2020).

30. L. Ye, Y. Yang, Z. H. Hang, C. Qiu, and Z. Liu, "Observation of valley-selective microwave transport in photonic crystals," Appl. Phys. Lett. **111**, 251107 (2017).

31. J. Noh, S. Huang, K. P. Chen, and M. C. Rechtsman, "Observation of photonic topological valley Hall edge states," Phys. Rev. Lett. **120**, 063902 (2018).

32. Y. T. Yang, H. Jiang, and Z. H. Hang, "Topological valley transport in two dimensional honeycomb photonic crystals," Sci. Rep. **8**, 1588 (2018).

33. J. Ma, X. Xi, and X. Sun, "Topological photonic integrated circuits based on valley kink states," Laser Photon. Rev. **13**, 190087 (2019).

34. X. L. Qi, Y. S. Wu, and S. C. Zhang, "General theorem relating the bulk topological number to edge states in two-dimensional insulators," Phys. Rev. B **74**, 045125 (2006).

35. R. S. Mong and V. Shivamoggi, "Edge states and the bulk-boundary correspondence in Dirac Hamiltonians," Phys. Rev. B **83**, 125109 (2011).

36. D. Xiao, M. C. Chang, and Q. Niu, "Berry phase effects on electronic properties," Rev. Mod. Phys. **82**, 1959–2007 (2010).

37. T. Fukui, Y. Hatsugai, and H. Suzuki, "Chern numbers in discretized Brillouin zone: efficient method of computing (spin) Hall conductances," J. Phys. Soc. Jpn. **74**, 1674–1677 (2005).

38. L. Zhang and S. S. Xiao, "Valley-Hall-like photonic topological insulators with vanishing Berry curvature," arXiv:1903.03338 (2019).

39. Z. Y. Li, L. L. Lin, and K. M. Ho, "Light coupling with multimode photonic crystal waveguides," Appl. Phys. Lett. **84**, 4699–4701 (2004).

40. H. J. Kim, I. Park, O. Beom-Hoan, S. G. Park, E. H. Lee, and S. G. Lee, "Self-imaging phenomena in multi-mode photonic crystal line-defect waveguides: application to wavelength de-multiplexing," Opt. Express **12**, 5625–5633 (2004).

41. I. Park, H. S. Lee, H. J. Kim, K. M. Moon, S. G. Lee, O. Beom-Hoan, S. G. Park, and E. H. Lee, "Photonic crystal power-splitter based on directional coupling," Opt. Express **12**, 3599–3604 (2004).